Influence of Oxide Formation Following Ultrashort Pulsed Laser Micromachining on Self-Propagating Reactions in Free-Standing Ni/Al Reactive Multilayer Foils

Maria Amélia Martins,* Christian Schäfer, Frank Mücklich, and Christoph Pauly

Reactive metallic multilayers, renowned for their exothermic self-propagating reactions, show a distinct ability to achieve minimal thermal influence in processes such as welding and soldering, where minimizing the thermal impact on the material being joined is crucial. Ultrashort pulsed lasers offer precision micromachining with negligible thermal damage, making them ideal for processing such sensitive materials. However, the formation and redeposition of oxide phases is a commonly observed side effect, especially when structuring in ambient air. This study investigates the effects of oxide formed after femtosecond laser treatment on self-propagating properties, including propagation velocity and microstructure of Ni/Al reactive multilayer foils. Samples with varied line spacings between laser-cut trenches are created. Scanning electron microscopy, high-speed camera videography, and image analysis are employed to analyze the microstructure and quantify velocities. Thermal simulations enhance the understanding of the oxide's role in self-propagating dynamics. The findings suggest that even a small oxide layer significantly decelerates the self-propagating reaction. The oxide functions as a thermal ballast by absorbing the thermal energy generated during the reaction, without actively participating in the reaction mechanism.

1. Introduction

Reactive metallic multilayers consist of a minimum of two alternating metallic layers, each with individual layer thickness ranging from approximately four up to several hundreds of nanometers and total film thickness up to several tens of microns.[1–9] These energetic materials are recognized for their ability to undergo exothermic self-propagating reactions upon local

ignition, characterized by a substantial amount of heat release within milliseconds,[4] and reaction front velocities reaching up to 100 m s^{-1}.[1] The self-propagating reaction can be initiated by electrical, mechanical, or thermal ignition mechanisms.[10] The reaction temperatures can exceed 2000 °C, depending on the system. Reactive multilayer systems have been extensively studied, with material combinations such as Ni/Al, Co/Al, Ru/Al, Nb/Si, Ti/Si, Pd/Al, and others identified and characterized over the years.[11–18] The foundation for the self-propagating reaction is the presence of one or more intermetallic phases in the respective phase diagram with a sufficiently large negative heat of formation.[19] Reactive multilayers can find diverse applications, including welding and soldering with high heat input for a very short time, leading to a minimum thermal influence. Additionally, they can serve as a heat source for secondary reactions,[20,21] and even for more cost-effective and energy-efficient manufacturing of metallic structures through additive manufacturing,[22] expanding their utility in diverse industrial and research contexts. A commercial product based on Ni/Al multilayers is available in the market and serves as sample material for the present study.

Ultrashort pulsed (USP) lasers are extensively used in high-precision micromachining across a wide range of materials, including metals,[23] ceramics,[24] and polymers.[25] The success of this machining process, characterized by superior surface quality and minimal damage to the workpiece, crucially relies on laser beam parameters. Pulsed lasers operating in the sub-picosecond regime show the capability to process reactive multilayers with minimal to no thermal damage.[11,26,27] This is attributed to the ultrashort duration of the pulses, during which atomic movement within the laser-affected zone is insignificant, allowing the atomic structure to remain intact.[28] Consequently, laser ablation utilizing femtosecond pulses yields clean features when compared to longer pulses. This capability enables high-quality and precise processing of sensitive materials with a negligible heat-affected zone (HAZ).[29–33] Precision cutting offers the ability to modify the geometry of the reactive foils, shaping the front propagation, and tailoring the reaction dynamics. Laser structuring offers promising potential in this regard. For instance, in the context of joining dissimilar materials such

M. A. Martins, C. Schäfer, F. Mücklich, C. Pauly
Chair of Functional Materials
Saarland University
Campus D3.3, 66123 Saarbrücken, Germany
E-mail: maria.martins@uni-saarland.de

The ORCID identification number(s) for the author(s) of this article can be found under https://doi.org/10.1002/adem.202400215.

as metal and polymer, precise control over the reaction front could enable adjustments in the heat release, minimizing the risk of defects and ensuring joint integrity.[34] Strategic modifications to the reactive multilayer foil (RMF) geometry via laser micromachining could facilitate the optimization of the thermal profile to meet specific material joining requirements. A prior study demonstrated that due to the nature of femtosecond ablation, a Ni/Al RMF, identical to the one utilized in this research, using the same laser parameters, could be micromachined without triggering a self-propagating reaction. The extent of the HAZ was found to be less than 100 nm, and the presence of Al oxide redeposition was observed, prompting further investigation in the current study. Moreover, no evidence of localized combustion within the irradiated region was observed.[29]

It is well known that following laser ablation in ambient air, the treated sample becomes covered in a debris layer formed from redeposited matter.[35–38] The extremely short duration of the pulse leads to highly localized and intense heating of the material leading to localized melting and/or vaporization. For materials containing aluminum, the extreme conditions generated by the femtosecond laser can result in the formation of aluminum oxide.[39,40] This process involves the reaction of molten or vaporized aluminum with the oxygen present in the surrounding atmosphere. The newly formed oxide layer then accumulates on the material surface, creating a layer.[41] The specific characteristics of the oxide layer, such as thickness and adherence to the underlying material, can be influenced by various factors, including laser parameters, ambient conditions, and the composition of the material being irradiated. Previous findings have shown that the predominant oxide phase generated after femtosecond irradiation of Ni/Al nanofoil is rich in Al. The presence of Ni is observed not as a constituent of the oxide itself but rather in the form of Ni–Al inclusions.[29]

In the present study, the effects of femtosecond laser micromachining on the self-propagating reaction of free-standing Ni/Al RMFs are investigated. The goal is to understand how the oxide layer formed after laser treatment influences self-propagating properties such as propagation velocity and thermal profile when geometrical features of the RMF are in the order of the reaction front width, i.e., <100 μm. Laser parameters were consistently maintained, and samples with different line spacings between the laser-cut trenches were created. The microstructure of the material immediately after laser treatment and subsequent cleaning was analyzed by means of scanning electron and optical microscopy. The self-propagating reaction was recorded using a high-speed camera, and an image analysis methodology was employed to quantify the velocities at different points across the tested samples. Additionally, thermal simulations were conducted to enhance the understanding of the role played by the oxide in the self-propagating dynamics.

2. Experimental Section

Commercial freestanding Ni/Al Nanofoil RMFs from Indium Corporation (Clinton, NY, USA) with bilayer thickness of 50 nm and total thickness of 40 μm were used as samples. The multilayers are coated on both sides with a 1 μm thick layer of InCuSil (61.5 wt% Ag, 24 wt% Cu, and 14.5 wt% In).

These multilayers have an atomic ratio of 1:1, enabling fast heating of the multilayers to temperatures ranging from 1350 to 1500 °C, achieving reaction front velocities of 6 and 8 m s^{-1}, according to the manufacturer's specifications.[42]

For the laser micromachining, samples with 10 mm in height and 15 mm in width were mounted on a 3-axis, computer-controlled stage in ambient atmosphere. In order to minimize the redeposition of ablated material, a vacuum dust collector was used. A Solstice ACE Ti:Sapphire laser with a Gaussian beam shape from Spectra-Physics (Santa Clara, CA, USA) operating at 800 nm of wavelength and generating 150 femtoseconds (fs) of pulse duration at full width half maximum, with 1 kHz of repetition rate, 25 μJ pulse energy, and fluence of 8.5 J cm^{-2} was used to structure the RMFs. The beam was focused by an aspheric lens with a focal length of 26 mm, resulting in a focused spot size of ≈20 μm. The stage scanning speed was kept constant at 0.02 mm s^{-1}. Loosely bound oxide flakes were removed by ultrasonic cleaning in ethanol for 1 h.

The self-propagating reaction was characterized by means of high-speed videography. A high-speed camera Photron (Tokyo, Japan) FASTCAM SA-Z 2100 K recording at 210 k frames per second (fps) and a resolution of 256 × 128 pixels with 0.25 μs shutter speed and zoom optic Navitar 12x was used to record the reaction. This results in a field of view of 0.82 × 0.41 mm^2 and a pixel size of 3.2 μm. A high-speed pyrometer was used to acquire time-resolved temperature data of the reaction and subsequent cooling. The pyrometer has a sampling time of 70 μs and temperature range of 750–2000 °C. Samples of ≈15 × 10 mm^2 were mounted in a caliper and placed in the high-speed test rig for a top-view recording of the samples. Ignition was performed by an electrical spark on one side, which served as a heat source to ignite the foil. **Figure 1**a shows a top-view photograph of the sample used in this work, highlighting both the ignition and the laser structuring position. The propagation velocities in different regions of the sample were determined by manually tracking the reaction front between two consecutive frames for a length of ten frames, which was then divided by the time taken for the reaction to travel between those frames. The analysis was performed using the software ImageJ.[43]

A confocal laser scanning microscope (CLSM) LEXT OLS4100, Olympus (Shinjuku, Tokyo, Japan) in laser scanning and optical mode was used to image the surface. A scanning electron microscope/focused ion beam (SEM/FIB) instrument Helios G4 PFIB CXe, Thermo Fisher (Waltham, MA, USA) was used for surface imaging, FIB cross-sectioning, and selective oxide removal to investigate the effect of thermal ballast.

Thermal simulations were employed to obtain data that are experimentally unavailable or difficult to access, including the temperature profile and rate of heat release. Based on the FIB cross-sections of the laser-structured line, the oxide layer on the sidewall was modeled. The effect on the temperature distribution is extracted from the simulations. COMSOL Multiphysics version 5.1 was used as the simulation environment. The geometric model used is a simplified representation of the Ni/Al reactive foil, with various thicknesses of an oxide layer composed of 90% alumina and 10% Ni. The addition of Ni to the oxide is based on previous findings cited earlier, where Ni was identified in the form of Ni–Al inclusions within the oxide layer.[29] The two-dimensional model consists of a top view of one of
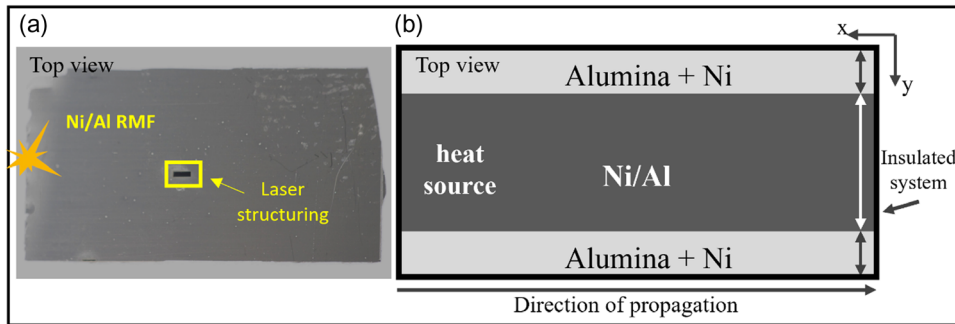
**ADVANCED
SCIENCE NEWS**
www.advancedsciencenews.com

**ADVANCED
ENGINEERING
MATERIALS**
www.aem-journal.com

Figure 1. Top-view schematics of Ni/Al RMF and reaction wave propagation: a) sample before the reaction, indicating the ignition site and the laser structuring position and b) schematic representation of the model of a single line used for the simulations with a moving heat source in the Ni/Al domain and two inert layers of oxide (alumina + Ni) on the sidewalls. The system was fully insulated.

the lines with 20 or 30 μm width with and without oxide layers of various thicknesses, resembling the view of the high-speed camera. The line length was set to 1 mm. The initial temperature of the system was assumed to be uniform at room temperature with a moving heat source applied only to the Ni/Al foil to initiate the self-propagating reaction, as illustrated in Figure 1b. The simulations assumed idealized conditions once the reaction was initiated. The construction aimed to capture thermal behavior while simplifying the model for computational efficiency and practical application.

3. Results and Discussion

3.1. Self-Propagating Reaction in Free-Standing Laser-Structured Ni/Al Reactive Foil

The pattern with different line spacings between the laser-cut trenches on the Ni/Al reactive foil ranging from 20 to 100 μm is presented in **Figure 2**. The aim behind varying the distance between the trenches, referred to as line spacing, is to investigate the potential impact of small lateral dimensions of the RMF on the velocity of the self-propagating reaction. The light optical image shows oxide redeposition with high absorption around the trenches (Figure 2a). Using the confocal laser scanning mode of the microscope, a topographic image, less sensitive to low reflectivity, shows the trenches and the varied spacing in between (Figure 2b).

Figure 3 shows a series of still images of the propagating reaction. The complete reaction can be seen in Video S1, available in the Supporting Information. The high-speed videos were recorded at 210 k fps with a frame size of 3.2 μm, offering a high-resolution perspective. The total reaction time captured was 176 μs, providing a detailed insight view into the rapid and dynamic progression of the self-propagating reaction. The ignition process was initiated through an electrical spark, which is a controlled and reproducible means for triggering the reaction in a freestanding way. Observations from Figure 3a–e show the upward progression of the front within the laser-structured area until complete material reaction is achieved. Notably, when closely examining Figure 3b–d, a visible deceleration in the propagation of the reaction front is visible, particularly where the line spacings are smaller. This deceleration is most prominent in the cases of line spacings measuring 20 and 30 μm. In contrast, line spacings of 60 and 100 μm seem to show a noticeable faster front propagation.

For assessing the reaction speed, the manual tracker analysis was conducted. Velocity measurements were determined for the
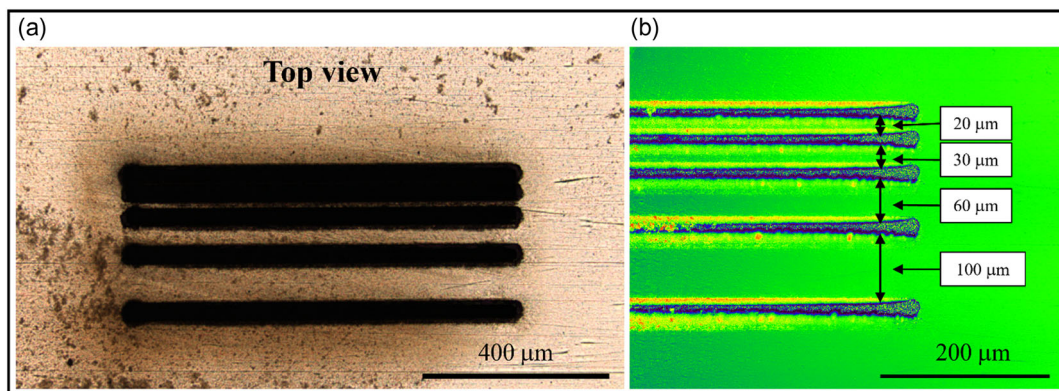

Figure 2. CLSM micrographs of the laser-patterned Ni/Al RMF without cleaning in the top view of the laser entry side: a) light optical image showing highly absorbing redeposition around the cut lines and b) topographic image showing the different line spacing (20, 30, 60, and 100 μm) as indicated by the arrows. All the lines penetrated through the 40 μm thickness of the foil.
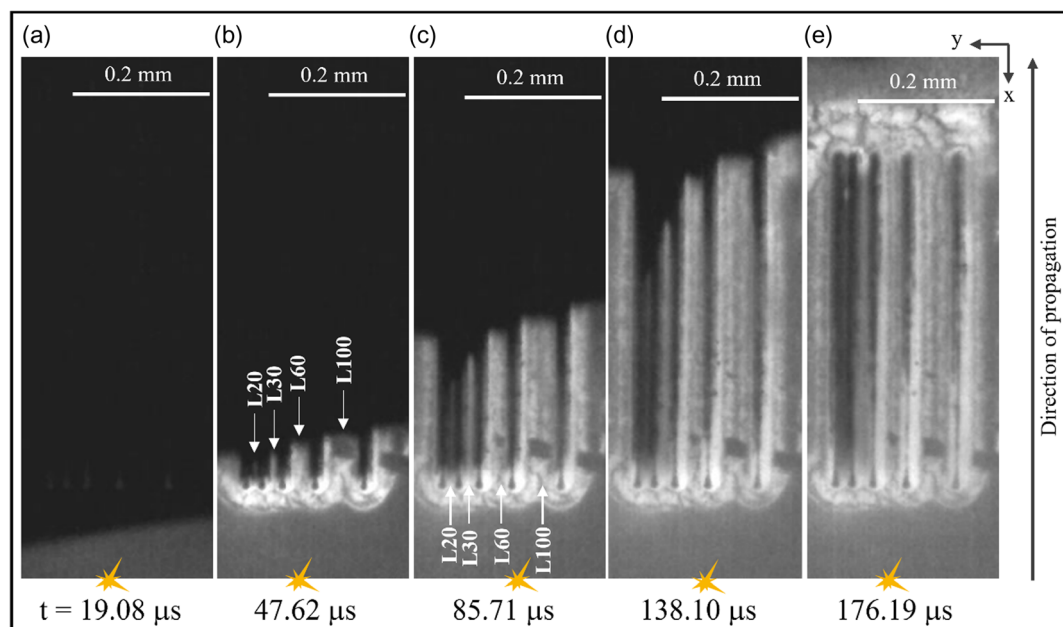
**ADVANCED
SCIENCE NEWS**

www.advancedsciencenews.com

**ADVANCED
ENGINEERING
MATERIALS**

www.aem-journal.com

Figure 3. Selected top-view still images from high-speed camera recordings of the sample with different line spacings: a) $t = 19.08$ μs, b) $t = 47.62$ μs with the front traveling within the structured area with different line spacings of 20 μm (L20), 30 μm (L30), 60 μm (L60), and 100 μm (L100), c) at the middle of the reaction ($t = 85.71$ μs), d) $t = 138.10$ μs, and e) at the end of the reaction ($t = 176.19$ μs). The yellow symbol represents the ignition point, and the direction of propagation is from bottom to top. The complete reaction can be seen in Video S1, Supporting Information.

unstructured regions of the sample and along the lines with 20, 30, 60, and 100 μm (**Figure 4**). Prior research has shown that the heat-affected zone after USP treatment primarily affects only ≈100 nm of the multilayer.[29] As a result, it can be inferred that even on a laser-treated foil, the multilayer remains largely unaffected a few microns away from the laser cutlines, and these areas were specifically chosen for measuring reaction velocity in the unstructured regions. A strong decrease in velocity for 20 and 30 μm line width is observed and even at 100 μm line width, the reduction is measurable.
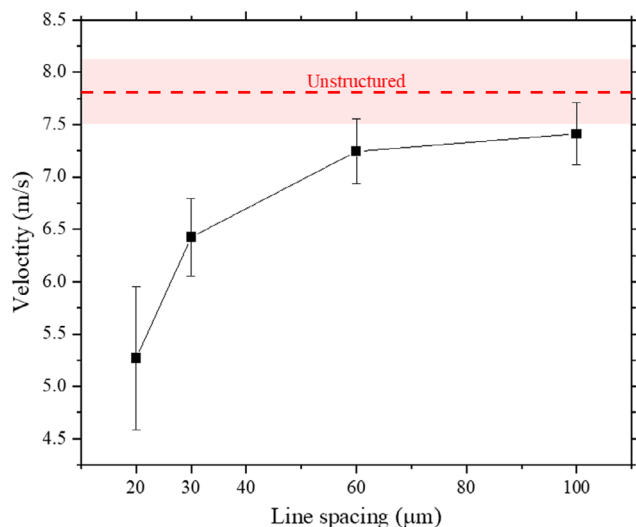

Figure 4. Front propagation velocities across the different line spacings.

At this point, it is unclear whether the reduced velocity is due to the line width approaching the size of the reaction front itself or if it is a result of the laser structuring process. A previous study investigated the oxide redeposition following laser irradiation, revealing the formation of a thick and hard-to-remove aluminum oxide layer on the line walls.[29] Additionally, a region of debris redeposition, extending ≈80 μm outside the trenches, was identified. However, those debris were easily removed by subjecting the sample to a 1-hour ultrasonic bath cleaning in ethanol. Hence, in addition to the amount of unreacted Ni/Al available ahead of the reaction front, the higher volume ratio of oxide-to-RMF for the smaller line spacings is likely a contributing factor to the observed deceleration of the reaction and this aspect will be comprehensively discussed in the following sections.

Following the observation of the impact of narrowing the line spacing previously shown, the line spacing of 30 μm was chosen for the further investigations of which parameters are playing a role in changing the speed of the reaction. **Figure 5**a presents a top view of the pattern created by laser structuring. For a better understanding of the influence of the oxide layer on the velocity and to have a direct comparison within the same sample, the oxide on both sides of one line was removed by FIB milling on a length of 0.8 mm. The cleaned line among the other three other ones with oxide on both sides (Lines 1, 2, and 3) can be seen in Figure 5b.

The internal structure of a second, identical RMF sample before the FIB-cleaning process was investigated. **Figure 6** presents an overview of the FIB cross-section extending through the entire thickness of one of the lines. In Figure 6b, a detailed view of the cross-section shows the cut edges, the distinct multilayer structure, and a noticeable compact layer of oxide covering
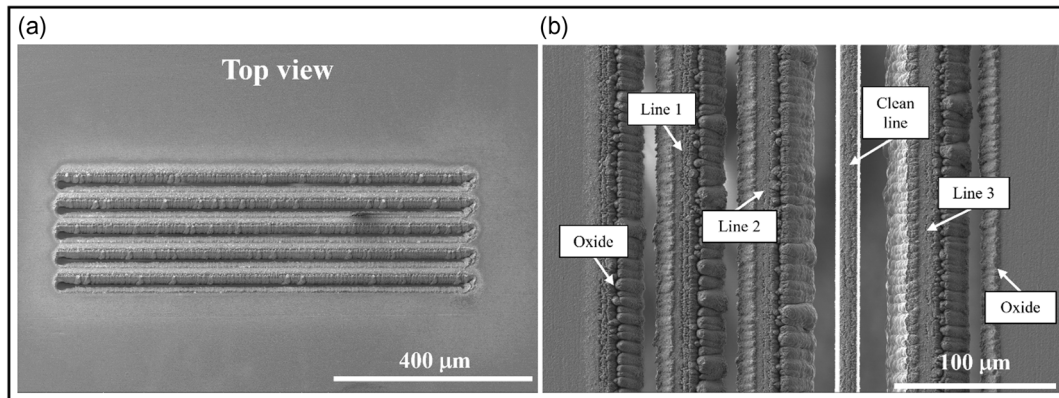
**ADVANCED
SCIENCE NEWS**

www.advancedsciencenews.com

**ADVANCED
ENGINEERING
MATERIALS**

www.aem-journal.com

Figure 5. Top-view SEM micrographs of laser entry side of the sample with constant 30 μm line spacing: a) after ultrasonic bath cleaning and b) close-up of the laser cut showing lines 1, 2, and 3 with oxide and the FIB-cleaned line free of oxide.
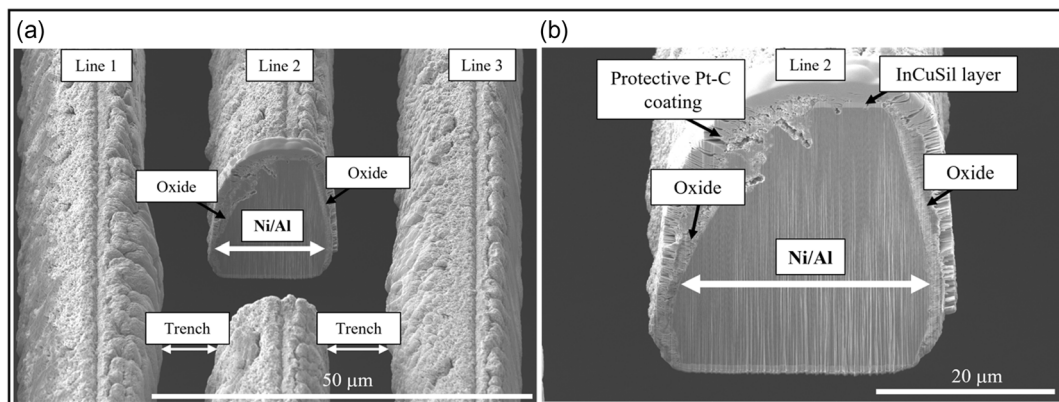

Figure 6. FIB cross-section of one laser-cut line: a) overview of lines 1 and 3 with cross-section of line 2 and b) detailed cross-section of line 2 featuring oxide layer, Ni/Al multilayer, and InCuSil layer as highlighted by arrows.

the ablation zone on both sides of the trenches. The thickness of the oxide layer varied across the different regions of the sample, ranging from 0.5 to 2.6 μm, while the multilayer exhibited a width between 10 and 29 μm. Additionally, the InCuSil layer is evident at both the top and bottom of the multilayer, indicating that there was no laser ablation within those regions.

After the FIB cleaning procedure, in a similar fashion to the sample with different line spacing (Figure 3), the sample was also taken to the test rig for high-speed videography, and the reaction was recorded at 210 k fps, with a pixel size of 3.2 μm and total reaction time of 186 μs. The propagation of the reaction front is shown in **Figure 7**a–e offering a detailed view of the beginning, middle, and end of the reaction. The complete reaction is shown in video S2, Supporting Information. Particularly, when observing the front propagation through the laser-structured area, especially in Figure 7b–d where the three lines with oxide (LO1, LO2, and LO3) are visible alongside a line free of oxide (LC), it becomes evident that the reaction front moves significantly slower within the lines containing an oxide layer within their trenches compared to the clean line and the surrounding unaffected regions both above and below the laser-structured area. This behavior remains consistent throughout the entire duration

of the reaction as it travels across the laser-cut region, shedding light on the influence of oxide presence on the self-propagating dynamics.

Upon close examination of velocity measurements, conducted using the same methodology as employed in the preceding sample, **Figure 8** reveals a significant deceleration of the reaction within the lines containing oxide. In contrast, the clean line (LC) and regions of the sample unaffected by laser irradiation (beginning and outside the structure) exhibit similar velocities, aligning with those seen for the standard Ni/Al, without any laser treatment. The outcome of this velocity analysis provides clarification for earlier assumptions regarding the sample with different line spacings (Figure 3), indicating that the oxide formed post-laser irradiation, assumed to be alumina, which is the most stable form of aluminum oxide, plays a significant role in on the self-propagating kinetics of the reaction.

FIB cross-sections were performed perpendicular to the sample surface for both the line with oxide and the clean line post-reaction, as illustrated in **Figure 9**. To reduce the effect of curtaining, pronounced by the challenging geometry of the reacted sample that prevented the sample from being coated with platinum, an image correction was carried out using an
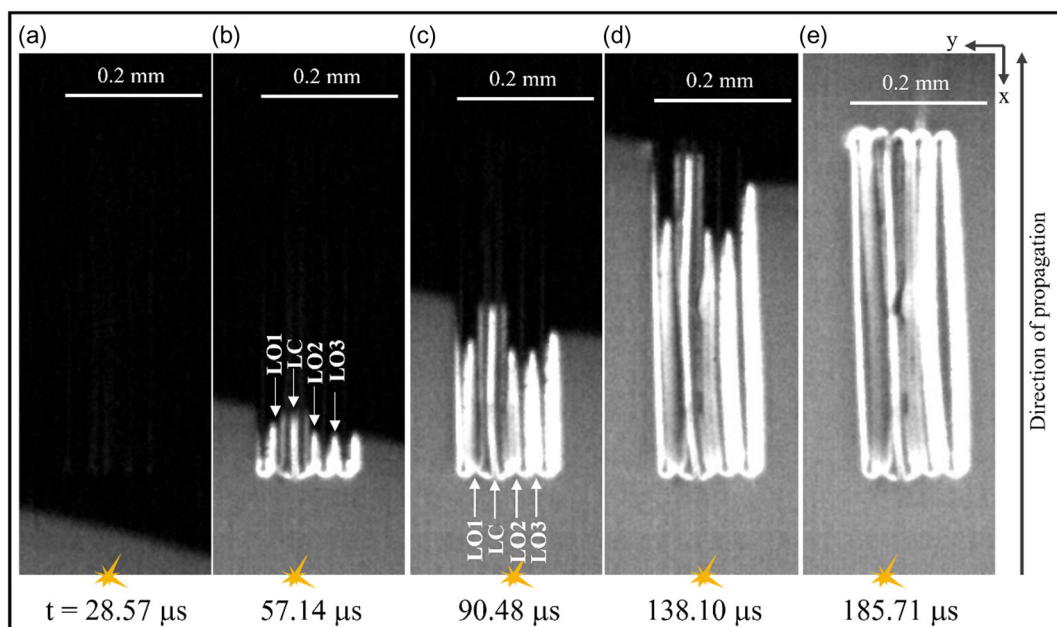
Figure 7. Top-view still images from high-speed camera recordings at selected times throughout the reaction for the sample with 30 μm of line spacings: a) $t = 28.57$ μs, b) $t = 57.14$ μs with the front traveling within the structured area within the lines with oxide (LO1, LO2, and LO3) and the FIB-cleaned line (LC), c) at the middle of the reaction ($t = 90.48$ μs), d) $t = 138.10$ μs, and e) at the end of the reaction ($t = 185.71$ μs). The yellow symbol represents the ignition point, and the direction of propagation is from bottom to top.
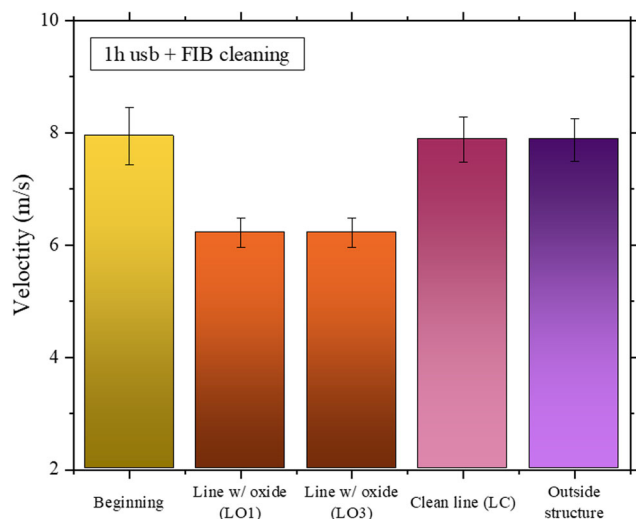

Figure 8. Front propagation velocities across different regions of the sample with 30 μm of line spacing. The reaction front velocity along the FIB-cleaned line is identical to that in the unstructured RMF.

algorithm for computing the variational signal-to-noise ratio.[44–46] Examining the cross section after reaction, it is not possible to see notable distinctions in the microstructure between the line with oxide (Figure 9a) and the clean line (Figure 9b). The grain size seems comparable in both cases suggesting that, at a microscopic level, the presence of oxide within the trenches and the subsequent cleaning process do not induce significant alterations in the material's microstructure.

3.2. Thermal Simulations

To explore the influence of the oxide layer on the heat distribution during self-propagating reaction in Ni/Al RMFs, finite element simulations were performed using COMSOL Multiphysics. By varying parameters such as the thickness of the oxide and velocity of the reaction according to the values obtained experimentally, the simulations were adapted to determine the temperature of the reaction fronts.

The simulations are based on the solution of the time-dependent heat conduction model, as shown in Equation (1), where ρ is the density, C_p is the heat capacity, k is the temperature-dependent heat conductivity, and Q is a normalized Gaussian-shaped moving heat source. The thermophysical parameters were defined based on homogenization using rule of mixture and relevant literature values, as shown in **Table 1**.

$$\rho C p \frac{\partial T}{\partial t} - \nabla(k \nabla T) = Q \qquad (1)$$

Equation (2) illustrates the Gaussian-shaped heat source employed for igniting the self-propagating reaction at the left end of the multilayer. In the equation, A represents a prefactor (2.8×10^{10} W m^{-3}), adjusted to match the maximum temperature (T_{max}) of the standard foil obtained experimentally. The standard deviation (σ) taken from ref. [47] is the width of the reaction front (25 μm) for the bilayer thickness given here. The variable v was varied based on experimentally measured velocities ranging from 6.2 to 7.9 m s^{-1}, while t represents time and x is the spatial coordinate.
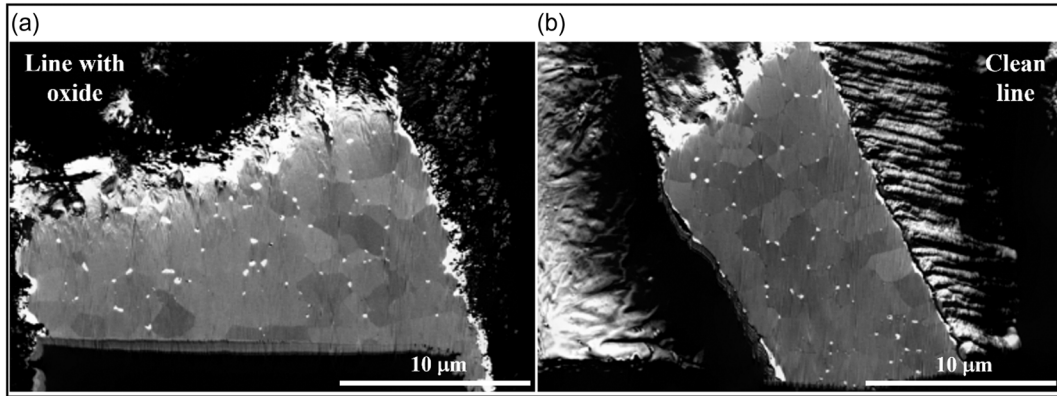
Figure 9. FIB cross-section of the reacted sample with 30 μm line width: a) grain size of the line with oxide and b) grain size of the cleaned line.

Table 1. Thermophysical properties of the components used for the simulations are based on calculations and literature. Temperature-dependent thermal conductivity of Ni/Al and alumina at ≈1300 °C extracted from refs. [47,52] respectively.

Property	Ni[52]	Al[52]	Ni/Al	Alumina[52]	90% Alumina + 10% Ni
Density (ρ) [kg m^{-3}]	8900	2700	5800	3800	4310
Thermal conductivity (k) [W (m K)$^{-1}$]	90.7	237	106[47]	6	14.5
Specific heat (C_p) [J (kg K)$^{-1}$]	445	897	671	880	836.4

$$Q_{(x,t)} = A \times \frac{1}{\sqrt{2\pi}\sigma} \times \exp\left(-\frac{1}{2}\frac{v \times t - x}{2\sigma}\right)^2 \qquad (2)$$

To investigate the influence of oxide thickness on the heat distribution within the Ni/Al foil, simulations were performed by varying the oxide layer (90% alumina, 10% Ni) thickness. The base simulation featured a 30 μm wide Ni/Al foil without the oxide layer, serving as a calibration for the calculations and representing the standard configuration before laser irradiation. Subsequent simulations introduced oxide layers with thicknesses ranging from 0.5 to 20 μm, as shown in **Figure 10**. The initial values were selected based on experimental observations, which indicated that the oxide layer from the sample with 30 μm of line spacing ranged from 0.5 to 2.6 μm, as presented in Figure 6. In Figure 10a–f, it can be observed that increasing the thickness of the oxide layer leads to a decrease in maximum temperatures.

To obtain the temperature profile of the reaction front at the midpoint of the reaction, point probes were placed. One probe was positioned in the center of the Ni/Al domain, while two others were placed in the center of the oxide layers, one at the top and the other at the bottom, as shown by the three dots in Figure 10f. **Figure 11** illustrates the changes in temperature behavior from the standard pure Ni/Al foil to the addition of oxide layers. For the simulation, the velocities used were taken from experimentally obtained values. The average velocity for the standard foil is 7.9 m s^{-1}, while for the domains with oxide, the velocity corresponds to the one of the line with oxide, measuring 6.2 m s^{-1}. For oxide thicknesses as thin as 0.5 and 2.5 μm, which are the thicknesses measured experimentally, a decrease in maximum temperature is observed compared to the standard foil, with the temperature profiles for both foil and oxide following

the same pattern. However, with a 5 μm oxide layer, a change in profile behavior already becomes evident. Not only is the maximum temperature lower, but it also takes more time for the oxide layer to reach the temperature of the foil. This is attributed to the insulating effect of alumina,[48] which causes a more gradual and prolonged transfer of heat, contributing to the observed temporal differences in temperature profiles between the foil and oxide. Beyond 10 μm, this behavior becomes even more pronounced, with significantly lower temperatures reached by the foil and a longer duration of heat release to the oxide. High temperatures in the foil are crucial for sustaining the exothermic reaction, and a decrease in temperature leads to a reduced propagation rate, significantly increasing the risk of reaction quenching as the rate of heat losses to the material ahead may exceed the rate of heat generation within the reaction front.[16,49,50] Simulations were also conducted for a Ni/Al width of 20 μm, demonstrating consistent behavior as the one seen for 30 μm. For brevity, only the maximum temperatures from those simulations will be presented later.

These observations from experiment and simulation indicate that, in the context of laser-structured Ni/Al RMFs, alumina debris functions as a thermal ballast. As a material with lower thermal conductivity compared to other materials, including Ni/Al RMF,[51] alumina acts as a thermal insulator. It absorbs heat energy generated by the exothermic reaction, essentially working as a heat sink. However, it is crucial to note that while alumina absorbs heat, it remains a passive element, not actively participating in the chemical reaction initiated by the RMF.

When comparing the maximum temperatures reached by the foils with widths of 20 and 30 μm, with oxide layers ranging from 0 to 20 μm, as shown in **Figure 12**, a clear trend is seen. With an
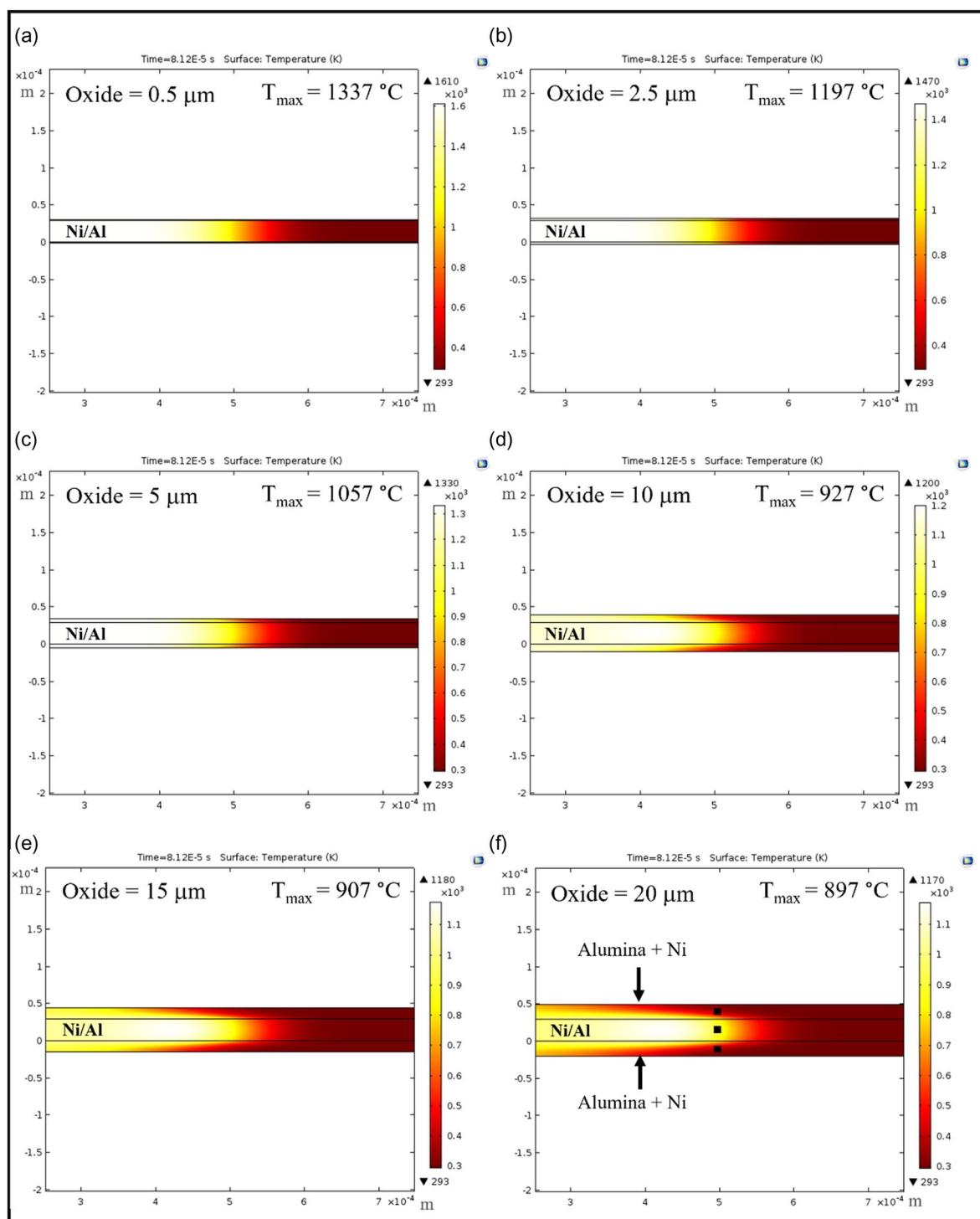
**ADVANCED
SCIENCE NEWS**

www.advancedsciencenews.com

**ADVANCED
ENGINEERING
MATERIALS**

www.aem-journal.com

Figure 10. Thermal simulations of the temperature distributions of a moving heat source ($v = 6.2\,\mathrm{m\,s^{-1}}$) in a 30-μm Ni/Al RMF in direct contact with an oxide layer (90% alumina, 10% Ni) with different thicknesses: a) 0.5 μm, b) 2.5 μm, c) 5 μm, d) 10 μm, e) 15 μm, and f) 20 μm. Arrows in this figure indicate the oxide layer and dots the probe positions. The configuration of the oxide and probe positions remained constant for all simulated thicknesses. Maximum temperatures (T_{max}) are reported in Celsius degrees. The view corresponds to a top view of the laser-structured samples.

increase in oxide thickness, there is a significant decrease in maximum temperatures for both Ni/Al widths. Even a thin oxide layer of 2.5 μm leads to a ≈300 °C reduction. This reduction correlates with the velocity measurements of the sample in which

one line was cleaned, while the other lines with oxide exhibited a slower reaction (Figure 8). As mentioned earlier, the observed temperature decrease is attributable to alumina's role in absorbing heat, which is gradually dissipated from the Ni/Al through
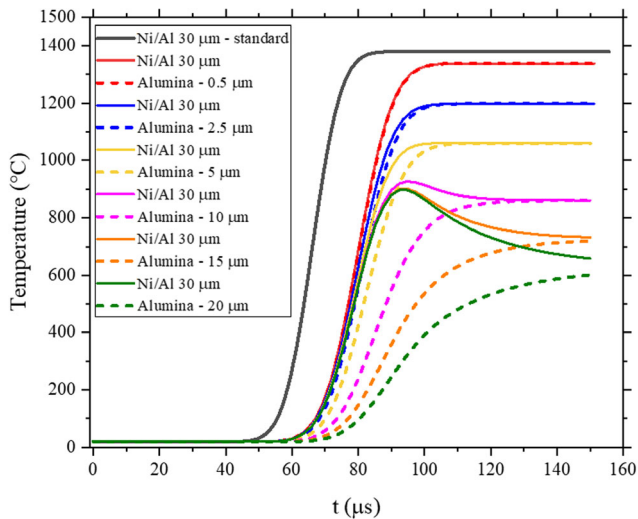
**ADVANCED
SCIENCE NEWS**

www.advancedsciencenews.com

**ADVANCED
ENGINEERING
MATERIALS**

www.aem-journal.com

Figure 11. Simulated temperature profile of a 30 μm wide Ni/Al foil and different oxide thicknesses ranging from 0.5 to 20 μm. Solid lines show profiles for probes positioned in the center of Ni/Al, while dashed lines represent profiles for probes in the center of the oxide layer. Velocities are based on experimental data: standard foil $v = 7.9\,\mathrm{m\,s^{-1}}$, and with oxide $v = 6.2\,\mathrm{m\,s^{-1}}$.

the oxide layer. Acting as a thermal ballast, alumina moderates the overall temperature rise in the Ni/Al RMF, as thermal energy is released over a longer period of time. The findings emphasize the crucial role of the oxide in influencing the dynamics of the self-propagating reaction, particularly in terms of propagation velocity, supporting earlier assumptions regarding the deceleration of the reaction front being related to the presence of the oxide layer.
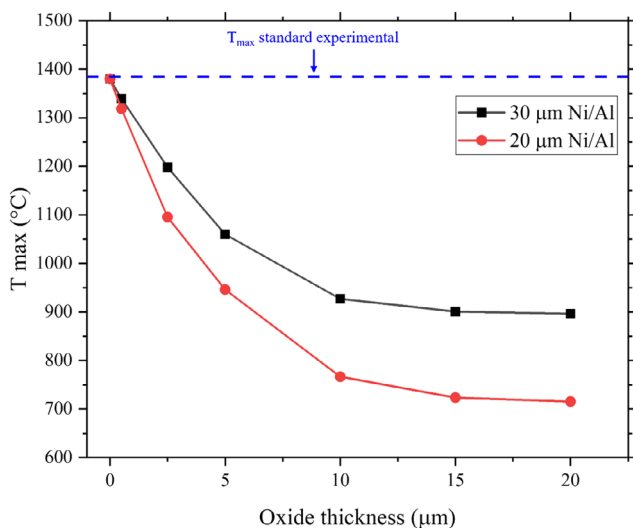

Figure 12. Maximum temperatures reached by the Ni/Al foils with 20 and 30 μm of width with 0, 0.5, 2.5, 5, 10, 15, and 20 μm of oxide layer added, and comparison with the maximum temperatures reached by the standard foil obtained experimentally.

4. Conclusion

This study presents the first attempt to investigate the impact of femtosecond laser micromachining on shaping the Ni/Al RMFs to tailor self-propagating reaction dynamics. Following femtosecond laser irradiation under ambient conditions, a substantial layer of oxide was produced and redeposited on laser-cut trench walls. The presence of oxide significantly decelerated the front propagation of the reaction. Functioning as a thermal ballast, the oxide absorbed thermal energy, thereby reducing the foil temperature and slowing the exothermic chemical reaction. In conclusion, even a thin oxide layer, as thin as 0.5 μm, was able to affect the front propagation. Nevertheless, for thicknesses exceeding 10 μm, the oxide thickness appeared to no longer play a significant role for the line widths investigated here. The presence of thermal ballast on a RMF structure proved to become relevant for small dimensions that could occur when downscaling reactive materials for micro-joining applications.

Supporting Information

Supporting Information is available from the Wiley Online Library or from the author.

Conflict of Interest

The authors declare no conflict of interest.

Data Availability Statement

The data that support the findings of this study are available from the corresponding author upon reasonable request.

[1] D. P. Adams, *Thin Solid Films* **2015**, *576*, 98.

[2] A. S. Rogachev, *Russ. Chem. Rev.* **2008**, *77*, 21.

[3] J. Wang, E. Besnoin, A. Duckham, S. J. Spey, M. E. Reiss, O. M. Knio, M. Powers, M. Whitener, T. P. Weihs, *Appl. Phys. Lett.* **2003**, *83*, 3987.

[4] B. Boettge, J. Braeuer, M. Wiemer, M. Petzold, J. Bagdahn, T. Gessner, *J. Micromech. Microeng.* **2010**, *20*, 064018.

[5] J. Braeuer, T. Gessner, *J. Micromech. Microeng.* **2014**, *24*, 115002.

[6] A. J. Gavens, D. Van Heerden, A. B. Mann, M. E. Reiss, T. P. Weihs, *J. Appl. Phys.* **2000**, *87*, 1255.

[7] A. S. Rogachev, A. S. Mukasyan, *Combust. Explos. Shock Waves* **2010**, *46*, 243.

[8] Q. Bizot, O. Politano, A. A. Nepapushev, S. G. Vadchenko, A. S. Rogachev, F. Baras, *J. Appl. Phys.* **2020**, *127*, 145304.

[9] A. S. Rogachev, S. G. Vadchenko, F. Baras, O. Politano, S. Rouvimov, N. V. Sachkova, M. D. Grapes, T. P. Weihs, A. S. Mukasyan, *Combust. Flame* **2016**, *166*, 158.

[10] G. M. Fritz, S. J. Spey, M. D. Grapes, T. P. Weihs, *J. Appl. Phys.* **2013**, *113*, 014901.

[11] Y. N. Picard, D. P. Adams, S. M. Yalisove, *Mater. Res. Soc. Symp. Proc.* **2005**, *850*, 115.

[12] K. Woll, I. E. Gunduz, C. Pauly, C. C. Doumanidis, S. F. Son, C. Rebholz, F. Mücklich, *Appl. Phys. Lett.* **2015**, *107*, 073103.

[13] C. Pauly, K. Woll, B. Bax, F. Mücklich, *Appl. Phys. Lett.* **2015**, *107*, 113104.

[14] C. Pauly, K. Woll, I. Gallino, M. Stüber, H. Leiste, R. Busch, F. Mücklich, *J. Appl. Phys.* **2018**, *124*, 195301.

[15] Maj, J. Morgiel, M. Szlezynger, *Int. J. Mater. Res.* **2019**, *110*, 60.

[16] S. Danzi, M. Menétrey, J. Wohlwend, R. Spolenak, *ACS Appl. Mater. Interfaces* **2019**, *11*, 42479.

[17] A. Cavaleiro, Ph.D. Thesis, University of Coimbra, Portugal **2014**.

[18] A. J. Cavaleiro, R. J. Santos, A. S. Ramos, M. T. Vieira, *Intermetallics* **2014**, *51*, 11.

[19] T. P. Weihs, *Handbook Thin Film Process Technology*, IOP Publishing, Bristol **1997**.

[20] S. Q. Arlington, G. M. Fritz, T. P. Weihs, *Annu. Rev. Mater. Res.* **2022**, *52*, 219.

[21] A. Wang, I. Gallino, S. S. Riegler, Y.-T. Lin, N. A. Isaac, Y. H. Sauni Camposano, S. Matthes, D. Flock, H. O. Jacobs, H.-W. Yen, P. Schaaf, *Mater. Des.* **2021**, *206*, 109790.

[22] R. Liu, C. Gao, A. Hou, S. Wang, *J. Mater. Process. Technol.* **2023**, *321*, 118167.

[23] A. Ancona, S. Döring, C. Jauregui, F. Röser, J. Limpert, S. Nolte, A. Tünnermann, *Opt. Lett.* **2009**, *34*, 3304.

[24] E. G. Gamaly, A. V. Rode, B. Luther-Davies, V. T. Tikhonchuk, *Phys. Plasmas* **2002**, *9*, 949.

[25] S. Ravi-Kumar, B. Lies, X. Zhang, H. Lyu, H. Qin, *Polym. Int.* **2019**, *68*, 1391.

[26] D. Neely, R. Allott, B. Bingham, J. Collier, J. Greenhalgh, M. Michaelis, J. Phillips, C. R. Phipps, P. Mckenna, *Appl. Opt.* **2014**, *53*, I41.

[27] M. D. Shirk, P. A. Molian, *J. Laser Appl.* **1998**, *10*, 18.

[28] E. G. Gamaly, A. V. Rode, *Prog. Quantum Electron.* **2013**, *37*, 215.

[29] M. A. Martins, D. W. Müller, J. Schmauch, M. Glaser, J. P. Bergmann, F. Mücklich, C. Pauly, *Appl. Sci.* **2023**, *13*, 1.

[30] Y. N. Picard, D. P. Adams, J. A. Palmer, S. M. Yalisove, *Appl. Phys. Lett.* **2006**, *88*.

[31] S. I. Kudryashov, B. Gakovic, P. A. Danilov, S. M. Petrovic, D. Milovanovic, A. A. Rudenko, A. A. Ionin, *Appl. Phys. Lett.* **2018**, *112*, 023103.

[32] J. Cheng, W. Perrie, S. P. Edwardson, E. Fearon, G. Dearden, K. G. Watkins, *Appl. Surf. Sci.* **2009**, *256*, 1514.

[33] B. N. Chichkov, C. Momma, S. Nolte, F. Alvensleben, A. Tünnermann, *Appl. Phys. A Mater. Sci. Process.* **1996**, *63*, 109.

[34] M. Glaser, S. Matthes, J. Hildebrand, J. Pierre Bergmann, P. Schaaf, *Mater. Des.* **2023**, *226*, 111561.

[35] A. S. Ahmed, D. W. Müller, S. Bruyere, A. Holtsch, F. Müller, J. Barrirero, K. Brix, S. Migot, R. Kautenburger, K. Jacobs, J.-F. Pierson, F. Mücklich, *ACS Appl. Mater. Interfaces* **2023**, *15*, 36908.

[36] N. Zhou, S. Yuan, M. Gao, W. Zhang, J. Zhang, T. Hu, *J. Mater. Res. Technol.* **2023**, *26*, 3408.

[37] T. Fox, P. Maria Delfino, F. Cortés, C. Pauly, D. Wyn Müller, M. Briesenick, G. Kickelbick, F. Mücklich, *ChemNanoMat* **2023**, *9*, e202300314.

[38] D. W. Müller, T. Fox, P. G. Grützmacher, S. Suarez, F. Mücklich, *Sci. Rep.* **2020**, *10*, 3647.

[39] J. Long, M. Zhong, H. Zhang, P. Fan, *J. Colloid Interface Sci.* **2015**, *441*, 1.

[40] X. Li, C. Yuan, H. Yang, J. Li, W. Huang, D. Tang, Q. Xu, *Appl. Surf. Sci.* **2010**, *256*, 4344.

[41] A. M. Makarov, D. A. Gerashchenkov, P. A. Kuznetsov, V. V. Ryabov, O. S. Vasiliev, *J. Phys. Conf. Ser.* **2021**, *1758*, 012024.

[42] *Indium Corp.* **2021**, *86*, 580400.

[43] C. A. Schneider, W. S. Rasband, K. W. Eliceiri, *Nat. Methods* **2012**, *9*, 671.

[44] J. Fehrenbach, P. Weiss, C. Lorenzo, *IEEE Trans. Image Process.* **2012**, *21*, 4420.

[45] J. Fehrenbach, P. Weiss, *SIAM J. Imaging Sci.* **2014**, *7*, 613.

[46] P. Escande, P. Weiss, W. Zhang, *J. Math. Imaging Vis.* **2017**, *57*, 43.

[47] L. Alawieh, O. M. Knio, T. P. Weihs, *J. Appl. Phys.* **2011**, *110*, 013509.

[48] M. Schubert, N. Leupold, J. Exner, J. Kita, R. Moos, *J. Therm. Spray Technol.* **2018**, *27*, 870.

[49] Z. A. Munir, U. Anselmi-Tamburini, *Mater. Sci. Rep.* **1989**, *3*, 279.

[50] J. J. Moore, H. J. Feng, *Prog. Mater. Sci.* **1995**, *39*, 243.

[51] T. Shimizu, K. Matsuura, H. Furue, K. Matsuzak, *J. Eur. Ceram. Soc.* **2013**, *33*, 3429.

[52] W. M. Haynes, *CRC Press* **2010**, *90*.

2400215 (10 of 10)